Microtubular Gas Diffusion Electrode Based on Ruthenium-Carbon Nanotubes for Ambient Electrochemical Nitrogen Reduction to Ammonia

Xin Wei,[a] Dominik Vogel,[a] Laura Keller,[a] Stefanie Kriescher,[a] and Matthias Wessling*[a, b]

The drawback of the energy-intensive Haber-Bosch process promotes the research and development of alternative ammonia (NH_3) synthesis approaches. The electrochemical nitrogen (N_2) reduction reaction (eNRR) may offer a promising method to produce NH_3 independent of fossil-fuel-based hydrogen production. However, the low solubility and the low-efficiency mass transport of N_2 in aqueous electrolytes are still among the challenges facing the feasibility of eNRR. Herein, we demonstrate a microtubular ruthenium-carbon nanotube gas diffusion electrode (Ru–CNT GDE), for the first time, applying it to electrochemical NH_3 synthesis in an H-type cell under ambient conditions. The highest reported Ru-catalyzed NH_3 yield rate of 2.1×10^{-9} mol/cm^{2}s and high faradaic efficiency of 13.5% were achieved, showing the superior effect of Ru–CNT GDEs on the eNRR performance. This work provides a new approach for the design and fabrication of self-standing catalyst-loaded GDEs for eNRR.

Ammonia (NH_3) is an essential fertilizer for the agricultural field,[1] and also attracts attention as a promising energy carrier because of its high hydrogen energy density and no carbon dioxide (CO_2) emission at decomposition.[2] Nowadays, the Haber-Bosch process dominates the industrial NH_3 synthesis, consuming two percent of the worldwide annual fossil energy production to produce NH_3 under harsh conditions and resulting in substantial CO_2 emissions.[3] The electrochemical nitrogen (N_2) reduction reaction (eNRR) using water as a proton source is gaining attention as a potential alternative for the Haber-Bosch process to synthesize NH_3 using renewable energy under mild conditions. Meanwhile, the energy demand of the eNRR process was substantiated by the simulation to be lower than that of the Haber-Bosch process using coal as a proton source.[4] However, eNRR faces the extreme challenge of low reaction activity and intense competition of the hydrogen evolution reaction (HER) in an aqueous electrolyte due to the high bond energy of the triply bonded N_2 molecule (940.95 kJ/mol).[5] In recent years, significant progress has been achieved in the development of catalysts and the electrocatalytic mechanism for eNRR. Ruthenium (Ru), as a promising catalyst for the eNRR, has been well investigated in various particle sizes,[6] support materials,[5,7] complexes,[8] and bimetallic catalysts,[9] achieving a significant improvement of NH_3 yield rate (ranging from 2.6×10^{-13} to 7.1×10^{-10} mol/cm^{2}s) and faradaic efficiency (0.05% to 29.6%), as listed in Table S1. However, the low solubility and slow mass transport of N_2 still restrict the eNRR feasibility.[10] Although ionic liquids were reported to encounter less of an issue on the low N_2 solubility, the application of ionic liquids still suffers from many drawbacks such as toxicity and high cost in the process for use.[11] In aqueous electrolytes, gas diffusion electrodes (GDEs) are mainly considered a promising solution for gas-liquid electrochemical reactions to facilitate transport and distribute the gaseous reactants with low solubility. GDEs have been widely deployed in fuel cells and electrolyzers for the oxygen (O_2) or CO_2 reduction reactions.[12] Focusing on tubular GDEs, the high power density and low fabrication costs present their superiority in electrochemistry.[13] The use of metallic and carbon-based tubular GDE led to promising results in solid oxide fuel cells[14] and for the CO_2 reduction reaction.[13,15] Notably, microtubular GDEs consisting of carbon nanotubes (CNT) were reported with highly porous and electrically conductive properties for wastewater treatment[16] and O_2 reduction.[17] However, a few studies employed catalyst-modified plate-shaped GDEs in a flow cell for the eNRR process, and both the faradaic efficiency (ranging from 0.01 to 6.0%) and NH_3 yield (ranging from 0.02×10^{-10} to 11.4×10^{-10} mol/cm^{2}s) have room for improvement.[7a,18]

Here, we present, for the first time, a carbon-based GDE with a microtubular geometry assembled in an H-type cell for the electrochemical NH_3 synthesis in an aqueous electrolyte. The self-standing microtubular GDE was composed of Ru nanoparticles loaded on CNTs, where CNTs were applied as the gas diffusion layer and simultaneously as catalyst support. The highest reported Ru-catalyzed NH_3 yield rate of 2.1×10^{-9} mol/cm^{2}s and high faradaic efficiency of 13.5% were achieved using the Ru–CNT GDEs at 0 V vs. reversible hydrogen electrode (RHE) in 0.1 mol/L phosphate buffer solution (PBS) under ambient conditions. The significant eNRR performance was achieved attributed to the GDE application and the enhancement of the reactant transport. Additionally, the self-standing microtubular

[a] X. Wei, D. Vogel, Dr. L. Keller, Dr. S. Kriescher, Prof. Dr. M. Wessling
RWTH Aachen University, Chemical Process Engineering
Forckenbeckstr. 51, 52074 Aachen, Germany
E-mail: manuscripts.cvt@avt.rwth-aachen.de
[b] Prof. Dr. M. Wessling
DWI-Leibniz Institute for Interactive Materials
Forckenbeckstr. 50, 52074 Aachen, Germany

Supporting information for this article is available on the WWW under https://doi.org/10.1002/celc.202001370

geometry showed a beneficial contribution to promote eNRR performance in the H-type cell.

Ru–CNT nanoparticles were prepared by loading Ru nanoparticles on acid-pretreated CNT by the chemical reduction method using sodium borohydride ($NaBH_4$) in ethylene glycol (see Section S1).[19] Figure 1a shows the scanning transmission electron microscope (STEM, Hitachi SU-9000) image, which visualizes the synthesized Ru–CNT nanoparticles. The Ru nanoparticles were highly dispersed on the surface of the CNT nanoparticles with an average diameter of 2.05 ± 0.35 nm (inset of Figure 1a). The Ru mass loading of 5.0 wt% was measured by thermogravimetric analysis (TGA, Netzsch TG 209, Section S1), as shown in Figure S1.

The Ru–CNT microtubes were prepared following the schematic illustration in Figure 1b (see Section S2). Firstly, the Ru–CNT nanoparticles with Ru loading of 5.0 wt% (200 mg) were dispersed in 200 mL of deionized water (18.2 MΩ cm) containing 2 g Triton X-100 (Sigma-Aldrich).[20] Subsequently, the obtained suspension was filtrated through a microfiltration hollow fiber membrane (PP S6/2, Accurel) in dead-end filtration mode. The Ru–CNT nanoparticles were rejected inside the membrane to form a Ru–CNT cake layer. The permeate volume was controlled to regulate the rejected Ru–CNT mass density of 6 mg/cm^2, as described by Gendel et al..[20] After the subsequent wash and dry processes, the hollow fiber membrane was removed and the cake layer was obtained as the Ru–CNT microtubes (as shown in Figure 1c). The Ru loading on the Ru–CNT microtubes was calculated to be 0.3 mg/cm^2. Moreover, the CNT microtubes as a reference were prepared by the blank CNT nanoparticles following the same method. The microtubes were characterized by scanning electron microscope (SEM, Hitachi Table Top TM 3030 Plus) with energy-dispersive X-ray spectroscope (EDX, Bruker) and by field emission scanning electron microscope (FESEM, Hitachi S4800) (Figure 1 and Figure S2). A smooth and uniform outer surface with no cracks is observed in Figure 1d. Further, the interconnected three-dimensional (3D) porous structure composed of the Ru–CNT fibers is revealed at higher magnification (Figure 1e). The SEM image of the Ru–CNT microtubes (Figure 1f) demonstrates the formation of the hollow tubular geometry. Moreover, the elemental mapping data of Ru (Figure S3) on the outer surface and cross-section of the Ru–CNT microtubes confirmed the existence and the even distribution of ruthenium. Figure 1g shows the axial cross-section of the Ru–CNT microtube with a thickness of around 150 μm. Moreover, the FESEM image at higher magnification visualizes the porous network structure facilitating the N_2 transport (Figure 1h). The microtubular Ru–CNT GDEs, which can connect with the gas and power supplies, were obtained by assembling the Ru–CNT microtubes with a dead-end mode (see Section S2 and Figure S4).

Electrochemical measurements were carried out to evaluate the eNRR performance of the microtubular Ru–CNT GDEs (Section S3). For this purpose, a gas-tight H-type cell is used with a three-electrode configuration (Figure 2a). A cation exchange membrane (Fumapem F-14100, Fuma-tech GmbH) was placed between its two compartments to separate the anolyte and catholyte. A platinized titanium mesh (Wieland Edelmetalle GmbH) and a Hg/Hg_2SO_4 electrode (HgE10NSK7, Sensortechnik Meinsberg GmbH) were supplied as anode and reference electrode, respectively. A 0.01 mol/L H_2SO_4 solution

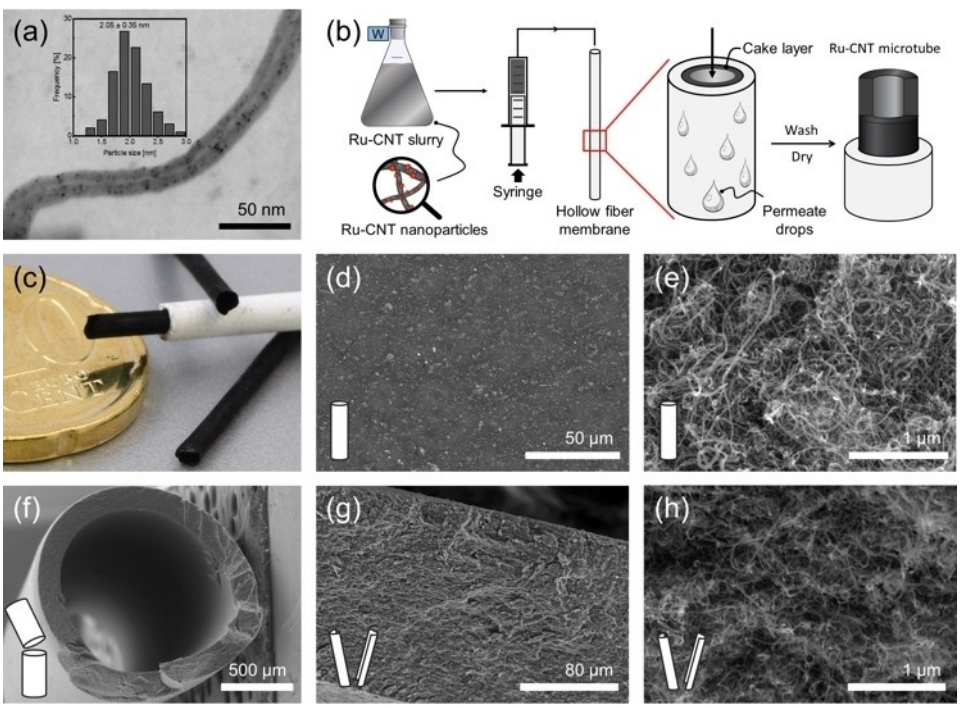

Figure 1. a) STEM image of Ru–CNT nanoparticles, the inset presents their particle size distribution. b) A schematic illustration of the Ru–CNT microtubes preparation. c) The photograph of the produced Ru–CNT microtubes. FESEM images of d, e) the outer surface, f) the radial cross-section, and g, h) the axial cross-section of the Ru–CNT microtube.

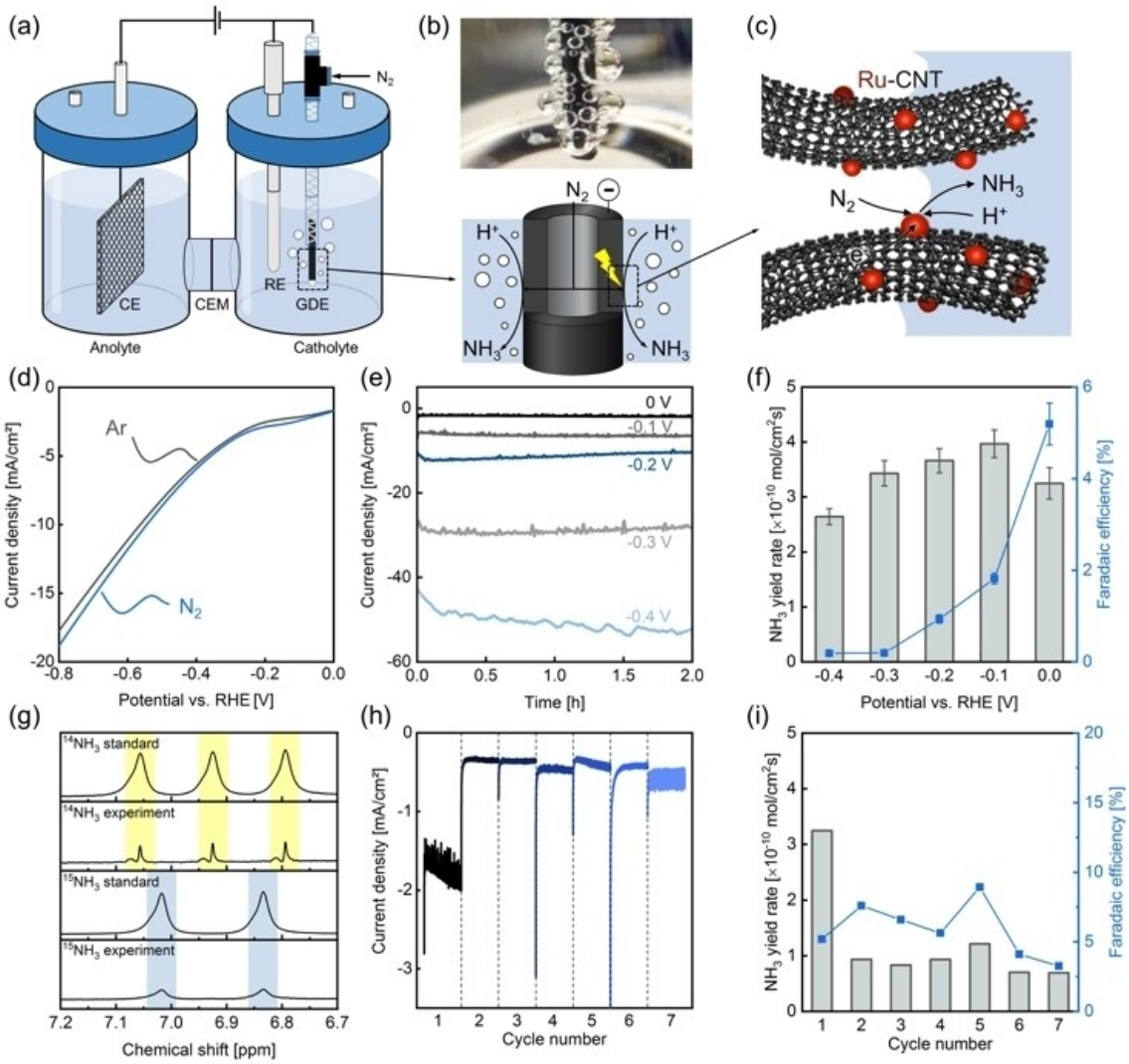

Figure 2. a) Schematic illustration of the eNRR process in the gas-tight H-type cell; b) the picture (top) and schematic (bottom) representation of the microtubular Ru–CNT GDE supplied with 0.3 bar N_2; c) the gas-electrolyte-catalyst three-phase interface reaction. d) LSV curves of the Ru–CNT GDE in Ar-saturated and N_2-saturated electrolyte (0.1 mol/L PBS) at a scan rate of 5 mV/s. e) The time-dependent current density curves for the Ru–CNT GDEs at various potentials (0, −0.1, −0.2, −0.3, and −0.4 V vs. RHE) for two hours, and f) the corresponding NH_3 yield rates (grey column) and faradaic efficiencies (blue point). g) ^{1}H NMR spectra obtained by the $^{14}NH_3$ and $^{15}NH_3$ standard samples and the PBS electrolytes after the electrolysis with using $^{14}N_2$ and $^{15}N_2$ as the feeding gas. The calibration of the chemical shifts in the spectra was conducted by DMSO as an internal standard. h) The time-dependent current density curves for the Ru GDE at 0 V vs. RHE for seven consecutive cycles, and i) the accompanying NH_3 yield rates (grey column) and faradaic efficiencies (blue point).

(100 mL) was used as anolyte and a 0.1 mol/L PBS (100 mL) as catholyte. The catholyte (pH of 7.2) consists of a mixture of monobasic dihydrogen phosphate (KH_2PO_4, Sigma-Aldrich) and dibasic monohydrogen phosphate (K_2HPO_4, Sigma-Aldrich). Before each electrolysis, the catholyte was pre-saturated with either N_2 (99.999%, Westfalen Austria GmbH) or argon (Ar, 99.999%, Westfalen Austria GmbH) for 30 minutes. In this work, the iR-compensated (85%) potentials were converted to the RHE scale. During the experiments, N_2 was purged into the microtubular GDEs with a constant pressure of 0.3 bar (Figure 2b), which results in a N_2 flow rate (average 0.48 mL/min) within two-hour electrolysis. The NH_3 production reaction takes place at the gas-electrolyte-catalyst three-phase interface, as shown in Figure 2c. The concentrations of produced NH_3 and N_2H_4 were spectrophotometrically detected after electrolysis by the indophenol blue method[21] and the Watt-Chrisp method[22] (Section S4 and S5). The corresponding standard absorbance and linear regression curves are illustrated in Figure S5 and S6. In this work, the produced H_2 was not investigated.

First of all, the electrochemical surface area (ECSA), based on the geometric area of the outside of the GDEs, was estimated based on the Randles-Sevcik equation[23] (Section S6, Figure S7). The Ru–CNT GDE achieved a four-time higher ECSA (9.3 cm^2) than the CNT GDE (2.3 cm^2), implying that the presence of the Ru nanoparticles improved the electrocatalytic performance. Additionally, compared to the geometric area, the significant ECSA compared to the geometry area suggests the blank CNT GDE as a promising gas diffusion substrate for the catalysts. The linear sweep voltammetry (LSV) measurement was conducted in N_2- or Ar-saturated electrolyte to investigate

the voltammetric behavior of the GDEs (Figure 2d). The LSV curve obtained in N_2-saturated electrolyte showed a slightly higher current density than the one in Ar-saturated electrolyte in the range from 0 to −0.8 V vs. RHE, implying an activity of the Ru–CNT GDE for the eNRR.[24]

The Ru–CNT GDEs were used to perform eNRR at various potentials from 0 to −0.4 with a step of 0.1 V vs. RHE for two hours. Figure 2e presents the time-dependent current density curves at different applied potentials. The current density was stable during the two-hour electrolysis at the potentials from 0 to −0.3 V vs. RHE. The current density obtained at −0.4 V vs. RHE increased slightly from 42.9 to 53.2 mA/cm^2. The slight fluctuation of the curves could originate from the produced H_2 bubbles at more negative potentials. Figure 2f shows the NH_3 yield rates (grey column) and the corresponding faradaic efficiencies (blue point) for all studied potentials. The NH_3 yield rate raised from 3.3×10^{-10} to 4.0×10^{-10} mol/cm^2 s by increasing the negative potential from 0 to −0.1 V vs. RHE. The NH_3 yield decreased gradually to 2.6×10^{-10} mol/cm^{2}s by further increasing the negative potential to −0.4 V vs. RHE. Furthermore, the faradaic efficiency decreased from 5.2% to 0.2% with increasing the negative potential from 0 to −0.4 V vs. RHE, which can be ascribed to the competitive HER becoming more dominant at a more negative potential. Consequently, the maximum NH_3 yield rate of 4.0×10^{-10} mol/cm^2 s (at −0.1 V vs. RHE) and faradaic efficiency of 5.2% (at 0 V vs. RHE) for the Ru–CNT GDE was achieved at low overpotential. Furthermore, N_2H_4 as a possible eNRR side-product was detected during all performance tests (Figure S8). The highest faradaic efficiency of 0.09% and the highest N_2H_4 yield rate of 5.0×10^{-12} mol/cm^2 s were obtained at 0 and −0.3 V vs. RHE, respectively.

To further verify that the detected NH_3 originates from the eNRR on the Ru nanoparticles, a series of the control experiments were conducted for two hours. First, electrolysis using the Ru–CNT GDE was conducted at open circuit potential (OCP) with N_2 supplied through the GDE. Second, the electrolysis using Ar as feed gas was tested by the Ru–CNT GDE at 0 V vs. RHE. Third, the CNT GDE was investigated with N_2 as feed gas at 0~V vs. RHE. The UV-vis absorption spectra (Figure S9) showed that only a trace amount of NH_3 was detected in the control experiments (Figure S9a-c) compared to the Ru–CNT GDE supplied with N_2 (Figure S9d) at 0 V vs. RHE. Concluding, no NH_3 was produced without the presence of the Ru catalyst, N_2, and potential. To further verify the N source of detected NH_3 in the electrolyte,[25] the $^{15}N_2$ isotope labeling experiment was performed in the setup with gas circulation (Figure S10) at −0.1 V vs. RHE in 0.1 mol/L PBS catholyte for two hours, as described in Section S7. The ^{1}H nuclear magnetic resonance (^{1}H NMR) spectra (Figure 2g) display a triplet coupling for $^{14}NH_4^+$ and a doublet coupling for $^{15}NH_4^+$ when $^{14}N_2$ and $^{15}N_2$ were supplied as the feeding gas. The result indicates the detected NH_3 originates from the Ru-catalyzed electroreduction of N_2. Moreover, NO_x as the possible contamination was verified to lead to a false-positive effect on eNRR; meanwhile, NO_x can be involved in the electrochemical system through the feeding gas, electrolytes (for instance, lithium sulfate), and the catalysts.[25–26] Hence, the possible presence of nitrate (NO_3^-) and nitrite (NO_2^-) involved in the electrochemical system was carefully investigated with the ion chromatography and the colorimetric test (see Section S8, Section S9; and the corresponding calibration samples in Figure S11 and Figure S12). Three samples were prepared for both NO_3^- and NO_2^- detection: (1) 100 mL original PBS catholyte, (2) 100 mL PBS catholyte with purging N_2 with a flow rate of 80 mL/min for 24 hours, (3) 100 mL PBS catholyte with bubbling N_2 through the Ru–CNT GDE at 0.3 bar for two hours. As a result, no significant absorbance increase for both NO_3^- and NO_2^- were recognized on the detection spectra in any case compared to the referencing sample deionized water (dash line), as shown in Figure S13. The results indicated that no significant presence of NO_x exists as an impurity in the system. Therefore, the detected NH_3 is confirmed to be produced by the electrochemical reduction of N_2 in this work.

Furthermore, the stability of the Ru–CNT GDE was investigated by 48 hour electrolysis at 0 V vs. RHE. A constant current density curve was achieved within the stability experiment, as shown in Figure S14. Besides, seven consecutive experimental cycles using the same Ru–CNT GDE were tested under the same conditions to investigate the reproducibility. After each experiment, the Ru–CNT GDE was washed under stirring in deionized water for two days and dried in a vacuum oven (35 °C and 40 mbar) for one day. Figure 2h illustrates the stable time-dependent current density curves within each repetitive two-hour electrolysis cycle. However, the average current densities degraded after the first cycle and then remained similar. Figure 2i shows the obtained NH_3 yield rates and faradaic efficiencies for each cycle. The yield rate degraded after the first cycle and stayed constant for the following cycles. However, the faradaic efficiencies remained in a range between 8.9% and 3.3%. By analyzing the GDE morphology, the degradation of the NH_3 yield rate after the first cycle could be explained as the pore blockage by the crystallization. The GDE after the experiment was microscopically characterized (Figure 3a and Figure S15a), indicating a non-homogeneous distribution of a crystal layer on the outer surface of the GDE. The uncovered areas correspond to the purple areas in the EDX elemental mapping of carbon distribution (Figure S15b), implying the original surface of the GDE. The EDX elemental mapping visualizes the coverage of the GDE with the crystal layer, composed of oxygen (O, Figure S15c), potassium (K, Figure S15d), and phosphorus (P, Figure S15e). These elements are the main components of catholyte (a mixture of KH_2PO_4 and K_2HPO_4, see Section S3). However, P and K were still present on the outer-surface and cross-section images of the GDE after washing two days in deionized water (Figure 3b-c and Fig-

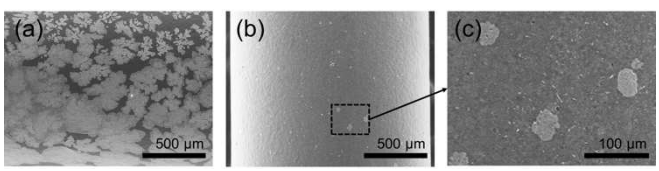

Figure 3. SEM images of the outer surface of the Ru–CNT GDEs after two-hour electrolysis: unwashed (a) and those washed whilst stirring in deionized water for two days at low magnification (b) and high magnification (c).

ure S16). The results imply that salt crystals formed remained at the surface and in the pores after the first experiment, which was not entirely removed by the washing process. The presence of the salt layer also reduces the mass transport of N_2 and, therefore, less N_2 can reach the active sites on the catalyst where the eNRR takes place. A further investigation of the applied electrolyte and the pore structure of GDEs is required to eliminate the shortcomings.

So far, the above achievements were obtained using Ru–CNT GDEs with a Ru loading of 0.3 mg/cm^2. To investigate the influence of the catalyst amount on the eNRR performance, the GDEs with various Ru loading were performed eNRR at 0 V vs. RHE for two hours. Therefore, GDEs with a Ru loading of 0.64 and 0.87 mg/cm^2 (Figure S1) were additionally prepared. Figure S17a shows the constant current density curves for the GDEs with different Ru loading and a higher Ru loading promotes the current density. Moreover, the highest NH_3 yield rate and faradaic efficiency were achieved by using the GDE with the highest Ru loading of 0.87 mg/cm^2 (Figure S17b), implying a positive effect of the significant Ru nanoparticle loading. To investigate the mass transport improvement by the GDE, the eNRR experiments were conducted using the Ru–CNT microtubes (0.87 mg/cm^2 Ru loading) with three different ways of gas supply at 0 V vs. RHE for two hours. Figure 4a demonstrates the ways of gas supply: (1) N_2 saturation of the atmosphere above the electrolyte (N_2 atm.); (2) N_2 supply into the electrolyte (N_2 in sol.); and, (3) N_2 supply through the GDE (N_2 in GDE). Thereby, the physically absorbed N_2 in the catholyte was electro-reduced to form NH_3 in configurations (1) and (2). In contrast, a three-phase boundary was created by using the Ru–CNT microtube as a GDE in configuration (3). A stable time-dependent current density of −4.4 mA/cm^2 was achieved by the configuration (3) with the gas supply through the GDE (Figure S18). However, the current densities decreased significantly from −22.8 to −1.0 mA/cm^2 by the configuration (1), and from −19.3 to −2.1 mA/cm^2 by the configurations (1) and (2) in the first hour. The apparent degradation of the current densities implied the diffusion limitation of N_2 into the electrolyte.[10] Figure 4b shows the mass change of the produced NH_3 during the electrolysis, which was recorded every 20 minutes. The NH_3 mass per geometric area of the electrodes linearly increased for the different ways of gas supply, whose linear regressions resulted in different slopes. The slopes are determined by linear regression (using OriginPro 2019) of the data points from 20 minutes on. The highest slope of 22.5 was obtained (3) by supplying the gas through the GDE, which was around 2.8 times higher than (2) by providing the gas into the electrolyte and almost 30 times higher than (1) by saturating the atmosphere above the electrolyte with N_2. Moreover, the eNRR results obtained using the three different configurations were displayed in Figure 4c. The electrolysis by purging N_2 through the GDE resulted in the highest NH_3 yield rate of 2.1×10^{-9} mol/cm^{2}s and faradaic efficiency of 13.5 %, compared with bubbling N_2 in the electrolyte and keeping N_2 atmosphere above the electrolyte. These results outperform the most reported Ru-catalyzed eNRR result (Table S1), highlighting the positive influence on the mass transfer by supplying the N_2 through the GDE.

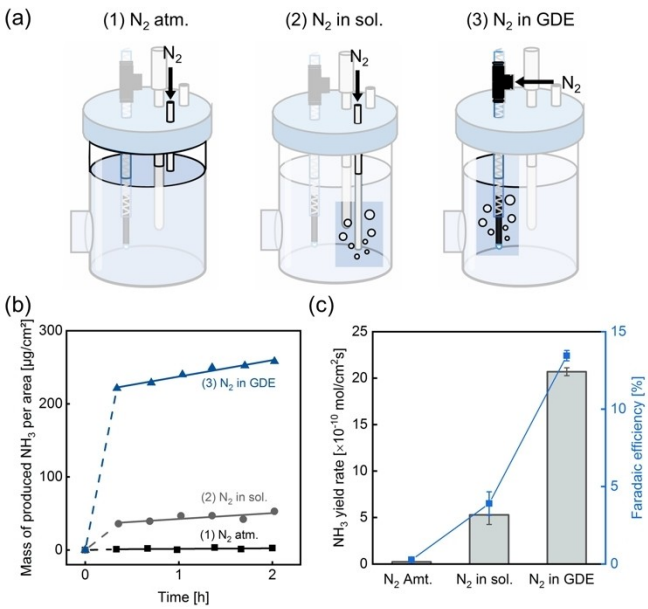

Figure 4. a) Schematic representations of the gas supply during the electrolysis: N_2 atmosphere (N_2 atm.) (1), bubbling N_2 in the catholyte (N_2 in sol.) (2), and bubbling N_2 through GDE (N_2 in GDE) (3). b) The NH_3 mass change per geometric electrode area using three different ways of N_2 supply (1. ■, 2. ● and 3. ▲) at 0 V vs. RHE. The solid lines present the accompanying linear regression curves. c) The corresponding NH_3 yield rates (grey column) and faradaic efficiencies (blue point).

In summary, a novel microtubular Ru–CNT GDE was demonstrated, for the first time, for the NH_3 synthesis under ambient conditions. The self-standing microtubular GDE assembled in an H-type cell was functioning as both the cathode and gas diffusion layer. The highest reported Ru-catalyzed NH_3 yield rate of 2.1×10^{-9} mol/cm^{2}s and high faradaic efficiency of 13.5 % were achieved using the Ru–CNT GDEs with a Ru loading of 0.87 mg/cm^2 in 0.1 mol/L PBS at 0 V vs. RHE. The remarkable results show the superior promotion of the Ru–CNT GDEs on the eNRR performance. By comparing with the typical electrolysis operation in the H-type cell, the application of GDE was proved to be imperative for the favorable reactant mass transport to promote eNRR. This work provides a new approach for designing and fabricating catalyst-loaded GDEs, which presents a beneficial improvement and ideal electrode support for catalyst-loaded evaluation assembled in the H-type cell towards eNRR.

Acknowledgements

This work was funded by the China Scholarship Council (CSC) under Grant 201608120054. The authors thank Karin Faensen for the SEM-EDX and FESEM measurements and Claudia Poerschke for the TGA measurements. Open access funding enabled and organized by Projekt DEAL.

Conflict of Interest

The authors declare no conflict of interest.

Keywords: electrochemical nitrogen reduction · ambient ammonia synthesis · microtubular gas diffusion electrode · ruthenium nanoparticles · mass transfer enhancement

[1] R. Schlögl, *Angew. Chem. Int. Ed.* **2003**, *42*, 2004–2008; *Angew. Chem.* **2003**, *115*, 2050–2055.
[2] a) S. Giddey, S. Badwal, A. Kulkarni, *Int. J. Hydrogen Energy* **2013**, *38*, 14576–14594; b) T. Vegge, R. Z. Sørensen, A. Klerke, J. S. Hummelshøj, T. Johannessen, J. K. Nørskov, C. Christensen, *in Solid-State Hydrogen Storage*, Elsevier, **2008**, pp. 533–564; cY. Bicer, I. Dincer, *J. Cleaner Prod.* **2018**, *170*, 1594–1601.
[3] G. F. Chen, S. Ren, L. Zhang, H. Cheng, Y. Luo, K. Zhu, L. X. Ding, H. Wang, *Small Methods* **2019**, *3*, 1800337.
[4] K. Kugler, B. Ohs, M. Scholz, M. Wessling, *Phys. Chem. Chem. Phys.* **2014**, *16*, 6129–6138.
[5] Z. Geng, Y. Liu, X. Kong, P. Li, K. Li, Z. Liu, J. Du, M. Shu, R. Si, J. Zeng, *Adv. Mater.* **2018**, *30*, 1803498.
[6] a) V. Kordali, G. Kyriacou, C. Lambrou, *Chem. Commun.* **2000**, 1673–1674; b) K. Kugler, M. Luhn, J. A. Schramm, K. Rahimi, M. Wessling, *Phys. Chem. Chem. Phys.* **2015**, *17*, 3768–3782; c) D. Wang, L. M. Azofra, M. Harb, L. Cavallo, X. Zhang, B. H. Suryanto, D. R. MacFarlane, *ChemSusChem* **2018**, *11*, 3416–3422; d) L. Zhao, J. Zhao, J. Zhao, L. Zhang, D. Wu, H. Wang, J. Li, X. Ren, Q. Wei, *Nanotechnology* **2020**, *31*, 29LT01.
[7] a) J. Nash, X. Yang, J. Anibal, J. Wang, Y. Yan, B. Xu, *J. Electrochem. Soc.* **2017**, *164*, F1712; b) B. H. Suryanto, D. Wang, L. M. Azofra, M. Harb, L. Cavallo, R. Jalili, D. R. Mitchell, M. Chatti, D. R. MacFarlane, *ACS Energy Lett.* **2018**, *4*, 430–435; c) S. Cheng, Y.-J. Gao, Y.-L. Yan, X. Gao, S.-H. Zhang, G.-L. Zhuang, S.-W. Deng, Z.-Z. Wei, X. Zhong, J.-G. Wang, *J. Energy Chem.* **2019**, *39*, 144–151; d) H. Tao, C. Choi, L.-X. Ding, Z. Jiang, Z. Han, M. Jia, Q. Fan, Y. Gao, H. Wang, A. W. Robertson, *Chem* **2019**, *5*, 204–214; e) B. Yu, H. Li, J. White, S. Donne, J. Yi, S. Xi, Y. Fu, G. Henkelman, H. Yu, Z. Chen, *Adv. Funct. Mater.* **2020**, *30*, 1905665; f) W. Peng, M. Luo, X. Xu, K. Jiang, M. Peng, D. Chen, T. S. Chan, Y. Tan, *Adv. Energy Mater.* **2020**, 2001364.
[8] a) B. M. Lindley, Q. J. Bruch, P. S. White, F. Hasanayn, A. J. Miller, *J. Am. Chem. Soc.* **2017**, *139*, 5305–5308; b) R. Zhao, C. Liu, X. Zhang, X. Zhu, P. Wei, L. Ji, Y. Guo, S. Gao, Y. Luo, Z. Wang, *J. Mater. Chem. A* **2020**, *8*, 77–81.
[9] a) Z. Wang, C. Li, K. Deng, Y. Xu, H. Xue, X. Li, L. Wang, H. Wang, *ACS Sustainable Chem. Eng.* **2018**, *7*, 2400–2405; b) H. Wang, Y. Li, D. Yang, X. Qian, Z. Wang, Y. Xu, X. Li, H. Xue, L. Wang, *Nanoscale* **2019**, *11*, 5499–5505; c) H. Wang, Y. Li, C. Li, K. Deng, Z. Wang, Y. Xu, X. Li, H. Xue, L. Wang, *J. Mater. Chem. A* **2019**, *7*, 801–805; d) Y. Li, H. Yu, Z. Wang, S. Liu, Y. Xu, X. Li, L. Wang, H. Wang, *Int. J. Hydrogen Energy* **2020**, *45*, 5997–6005; e) J. Wang, B. Huang, Y. Ji, M. Sun, T. Wu, R. Yin, X. Zhu, Y. Li, Q. Shao, X. Huang, *Adv. Mater.* **2020**, *32*, 1907112.
[10] C. Tang, S.-Z. Qiao, *Chem. Soc. Rev.* **2019**, *48*, 3166–3180.
[11] F. Zhou, L. M. Azofra, M. Ali, M. Kar, A. N. Simonov, C. McDonnell-Worth, C. Sun, X. Zhang, D. R. MacFarlane, *Energy Environ. Sci.* **2017**, *10*, 2516–2520.
[12] D. Higgins, C. Hahn, C. Xiang, T. F. Jaramillo, A. Z. Weber, *ACS Energy Lett.* **2018**, *4*, 317–324.
[13] R. Kas, K. K. Hummadi, R. Kortlever, P. De Wit, A. Milbrat, M. W. Luiten-Olieman, N. E. Benes, M. T. Koper, G. Mul, *Nat. Commun.* **2016**, *7*, 1–7.
[14] a) M. H. D. Othman, N. Droushiotis, Z. Wu, G. Kelsall, K. Li, *Adv. Mater.* **2011**, *23*, 2480–2483; b) M. H. D. Othman, Z. Wu, N. Droushiotis, U. Doraswami, G. Kelsall, K. Li, *J. Membr. Sci.* **2010**, *351*, 196–204.
[15] H. Li, N. Xiao, Y. Wang, C. Li, X. Ye, Z. Guo, X. Pan, C. Liu, J. Bai, J. Xiao, *J. Mater. Chem. A* **2019**, *7*, 18852–18860.
[16] H. Roth, Y. Gendel, P. Buzatu, O. David, M. Wessling, *J. Hazard. Mater.* **2016**, *307*, 1–6.
[17] Y. Gendel, H. Roth, A. Rommerskirchen, O. David, M. Wessling, *Electrochem. Commun.* **2014**, *46*, 44–47.
[18] a) R. Lan, J. T. Irvine, S. Tao, *Sci. Rep.* **2013**, *3*, 1–7; b) J. Kong, A. Lim, C. Yoon, J. H. Jang, H. C. Ham, J. Han, S. Nam, D. Kim, Y.-E. Sung, J. Choi, *ACS Sustainable Chem. Eng.* **2017**, *5*, 10986–10995; c) S. Chen, S. Perathoner, C. Ampelli, C. Mebrahtu, D. Su, G. Centi, *Angew. Chem. Int. Ed.* **2017**, *56*, 2699–2703; *Angew. Chem.* **2017**, *129*, 2743–2747; d) X. Yang, J. Nash, J. Anibal, M. Dunwell, S. Kattel, E. Stavitski, K. Attenkofer, J. G. Chen, Y. Yan, B. Xu, *J. Am. Chem. Soc.* **2018**, *140*, 13387–13391.
[19] a) F. Avilés, J. Cauich-Rodríguez, L. Moo-Tah, A. May-Pat, R. Vargas-Coronado, *Carbon* **2009**, *47*, 2970–2975; b) F. Wang, Y. Wang, Y. Zhang, Y. Luo, H. Zhu, *J. Mater. Sci.* **2018**, *53*, 6831–6841.
[20] Y. Gendel, O. David, M. Wessling, *Carbon* **2014**, *68*, 818–820.
[21] R. B. Willis, M. E. Montgomery, P. R. Allen, *J. Agric. Food Chem.* **1996**, *44*, 1804–1807.
[22] G. W. Watt, J. D. Chrisp, *Anal. Chem.* **1952**, *24*, 2006–2008.
[23] L. Wang, X. Lu, C. Wen, Y. Xie, L. Miao, S. Chen, H. Li, P. Li, Y. Song, *J. Mater. Chem. A* **2015**, *3*, 608–616.
[24] K. Kugler, S. M. Kriescher, M. Giela, S. Hosseiny, K. Thimm, M. Wessling, *Chem. Ing. Tech.* **2020**, *92*, 62–69.
[25] S. Z. Andersen, V. Čolić, S. Yang, J. A. Schwalbe, A. C. Nielander, J. M. McEnaney, K. Enemark-Rasmussen, J. G. Baker, A. R. Singh, B. A. Rohr, *Nature* **2019**, *570*, 504–508.
[26] L. Li, C. Tang, D. Yao, Y. Zheng, S.-Z. Qiao, *ACS Energy Lett.* **2019**, *4*, 2111–2116.

Manuscript received: October 27, 2020
Accepted manuscript online: November 9, 2020